

# Fe<sub>7</sub>S<sub>8</sub>/N-doped Graphene Foam Composite as Efficient Bifunctional Electrocatalysts for Overall Water Splitting

Xin Huang, Shuliang Wang\*, Xueli Zhang, Li Liu

School of New Energy and Materials, Southwest Petroleum University, Xindu Avenue 8#, Sichuan 610500, China

\*E-mail: [wsliang1465@126.com](mailto:wsliang1465@126.com)

Received: 5 January 2021 / Accepted: 3 February 2021 / Published: 28 February 2021

Exploring and developing efficient and stable bifunctional electrocatalysts for overall water splitting is of great importance to alleviate the serious consumption of fossil energy sources. Herein, nano-constructed iron sulfide loaded on N-doped graphene foam (Fe<sub>7</sub>S<sub>8</sub>/NGF) was obtained by hydrothermal process and chemical vapor deposition (CVD) and used as a highly efficient electrocatalyst for HER (hydrogen evolution reaction) and OER (oxygen evolution reaction). The graphene foam with a three-dimensional porous structure not only improves the overall conductivity of the catalyst but also facilitates the in-situ growth of Fe<sub>7</sub>S<sub>8</sub> nanoparticles and exposes more active sites, thereby optimizing mass and electron transfer. Therefore, the synergistic effect of transition metal sulfide and NGF has greatly enhanced its catalytic performance. In 1 M KOH, Fe<sub>7</sub>S<sub>8</sub>/NGF bifunctional electrocatalyst has excellent HER (197.8 mV, 10 mA·cm<sup>-2</sup>) and OER (450 mV, 100 mA·cm<sup>-2</sup>) catalytic ability as well as highly stability for long-term operation. Moreover, the Fe<sub>7</sub>S<sub>8</sub>/NGF catalyst exhibits excellent ability for overall water splitting, reaching a current density of 100 mA·cm<sup>-2</sup>, requires an additional applied voltage of 2.21 V only, and maintains good stability during 12 hours of continuous work.

**Keywords:** Bifunctional electrocatalysts; Iron sulfide; N-doped graphene foam; Hydrothermal process; Chemical vapor deposition.

## 1. INTRODUCTION

At present, humans are confronted with an increasingly severe energy crisis. Thus, renewable and environment-friendly alternative energy sources should be developed. Among numerous conversion systems and energy storage, an ideal electrolytic water technology has been favored by scholars and widely studied[1]. Water electrolysis includes two half reactions, namely, hydrogen evolution reaction (HER) and oxygen evolution reaction (OER). OER remains a challenging research direction because of its slow thermodynamic process and large overpotential[2]. Therefore, developing a catalyst with high catalytic activity, good stability, and appropriate cost for large-scale industrialization of decomposed

water is of great importance[3]. Platinum (Pt) and noble metal oxides, such as IrO<sub>2</sub> and RuO<sub>2</sub>, are highly efficient and considered state-of-the-art HER and OER catalysts. However, these noble metal catalysts are unfavorable for practical applications because of their scarcity and high cost[4, 5].

Researchers have explored and studied a variety of electrocatalysts, such as transition metal-based materials (chalcogenide[6, 7], phosphides[8], boride[9], and metal oxide/hydroxide[10-12]), and metal-free catalysts[13, 14]. Compared with other transition metal-based compounds, iron-based materials are advantageous for electrocatalytic applications[15-17] because iron is the second most abundant metal in the Earth's crust and has the lowest toxicity. Fe-S clusters are active centers of enzymes that catalyze some important biological reactions in nature. Iron sulfide has been reported as a high-efficiency electrocatalyst[16, 18] but not as a bifunctional electrocatalyst because its catalytic activity and stability are not as good as catalysts based on precious metals and other transition metals. The number of active sites are greatly reduced due to the inherent stacking and aggregation properties of individual transition metal sulfides[19]. To solve the above problems, scholars have developed an effective method that combines transition metal sulfides with three-dimensional carbon additives to not only reduce the stacking and expose more active sites but also enhance the conductivity of the electrocatalyst[20, 21]. Ling et al.[22] loaded Co<sub>1.097</sub>S nanoparticles on graphene foams to achieve excellent activity for water splitting. The current density of 10 mA·cm<sup>-2</sup> in OER and HER only requires overpotentials of 240 and 124 mV, respectively. Similarly, Zhao et al.[23] loaded MoS<sub>2</sub> nanosheets onto graphene aerogels to expose more active sites and enhance their HER catalytic capability.

Inspired by the above research, the present work fabricated Fe-S/NGF electrocatalysts by loading Fe-S nanoparticles on NGF. The carbon atoms in the lattice are replaced by nitrogen atoms in the conductive carbon substrate doped with nitrogen atoms, and sp<sup>2</sup> hybridization is destroyed. Nitrogen atoms with more negative charge give electrons to the system, thereby promoting the adsorption of intermediates on the surface of the electrocatalyst and the electron transfer during the catalytic reaction[24, 25]. In addition, the doping of N atoms inevitably introduces some inherent defects, such as point defects or disordered structures, which are beneficial to enhance the catalytic activity[26]. The unique three-dimensional structure greatly increases the contact area with the electrolyte and exposes more active sites.

## 2. EXPERIMENTAL

### 2.1 Materials

All chemicals were of analytical grade unless otherwise specified. Deionized water was used throughout the tests. Graphene oxide powder was provided by Nanjing XFNano Material Tech Co., Ltd. (Nanjing, China). CH<sub>4</sub>N<sub>2</sub>S (Thiourea), Fe(NO<sub>3</sub>)<sub>3</sub>·9H<sub>2</sub>O, C<sub>2</sub>H<sub>6</sub>O (Ethanol), and CH<sub>4</sub>N<sub>2</sub>O (Urea) were purchased from Chron Chemicals Co., Ltd. (Chengdu, China). Nafion solution (5 wt.%) was provided by DuPont, China.

## 2.2 Synthesis of electrocatalysts

Catalyst precursor was synthesized by hydrothermal method and sulfurized by chemical vapor deposition to obtain the target sample Fe-S/NGF-600. In brief, 0.15 g of graphene oxide powder was immersed in 30 ml of deionized water and sonicated for several hours until a uniform suspension was formed. The suspension was added with 2.25 mmol urea (AR) and 1.125 mmol  $\text{Fe}(\text{NO}_3)_3 \cdot 9\text{H}_2\text{O}$  (AR) and stirred for several minutes. The above suspension was placed into a 50 ml Teflon-lined stainless steel autoclave reactor and reacted at 180 °C for 12 h. After cooling to room temperature, the sample was collected, cleaned several times with deionized water, and freeze dried. Thiourea and the as-prepared sample were placed at the upstream and downstream sides of the furnace, respectively, and the mass ratio of thiourea to sample was 6:1. The tube furnace was controlled at 600 °C for 2 h with argon flow to obtain Fe-S/NGF-600. Figure 1 shows the schematic of the sample preparation.

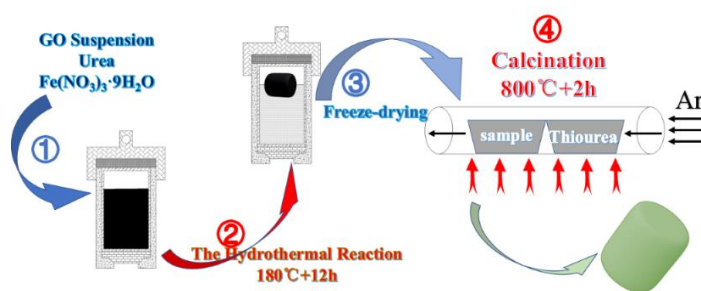


**Figure 1.** Synthesis of Fe-S/NGF composite

The samples were subjected to calcination temperatures of 400 °C and 800 °C to prepare Fe-S/NGF-400 and Fe-S/NGF-800 for comparison. Two other samples (Fe-S/NGF and Fe-S) were synthesized for comparison. Fe-S/NGF was prepared by two-step hydrothermal method. First, 0.25 g of graphene oxide powder was immersed in 50 ml of deionized water and sonicated for several hours to form homogeneous dispersion suspension. The suspension was then added with 0.6 g of urea under continuous stirring for 10 min. The prepared suspension was transferred into a 100 ml Teflon-lined stainless steel autoclave reactor and reacted at 180 °C for 12 h. After the furnace was cooled to room temperature, the sample was collected, cleaned several times with deionized water, and freeze dried. The sample was placed in a tube furnace and calcined at 800 °C for 2 h under an argon atmosphere to obtain nitrogen-doped graphene foam (NGF). Second, 4.375 mmol thiourea and 2.625 mmol  $\text{Fe}(\text{NO}_3)_3 \cdot 9\text{H}_2\text{O}$  were added into 70 ml of ethanol under stirring to form a homogeneous solution. The solution along with NGF was transferred into a 100 ml Teflon-lined stainless steel autoclave and reacted at 180 °C for 12 h. After the furnace was cooled to room temperature, the product was cleaned with deionized water for several times and dried in a vacuum oven at 60 °C. Fe-S was synthesized by the same process as Fe-S/NGF without the presence of NGF.

### 2.3 Characterization

The composition and surface morphology of the synthesized samples were characterized by scanning electron microscope (ZEISS EV0 MA15, Germany) equipped with energy dispersive spectrometer (EDS) at an acceleration voltage of 20 kV. Phase structures were analyzed using XRD (Bruker D8 advance) with Cu K $\alpha$  radiation ( $\lambda=0.154056$  nm). The element composition and valence of the sample was analyzed through X-ray photoelectron spectroscopy (XPS) using Thermo ESCALAB 250XI with efficiency and energy voltage of 12 kV, vacuum degree during sputtering of  $2.0 \times 10^{-7}$  mbar, and Mg K $\alpha$  target as the radiation source.

The electrochemical performance of the samples was tested in 1 M KOH solution at room temperature by using a Gmary Reference 3000 workstation. A classical three-electrode system was adopted with Ag/AgCl electrode as the reference electrode, Pt as the counter electrode, and sample directly coated on the nickel foam as the working electrode. The working electrode was prepared by adding 5 mg of the catalyst powder and 40  $\mu$ l of Nafion (5 wt%) in 1 ml of ethanol. The mixed suspension was sonicated for 30 min to form a homogeneous ink. The ink was dropped onto the precleaned nickel foam (1 cm  $\times$  1 cm) with a catalyst loading of  $\sim 5$  mg $\cdot$ cm $^{-2}$  and dried at room temperature. Linear sweep voltammetry (LSV) was performed on each group of samples to analyze and compare the catalytic performance of different samples. All applied potentials were converted with respect to reversible hydrogen electrode (RHE) by using the following formula:

$$E_{\text{RHE}}=E_{\text{Ag/AgCl}}+0.059\cdot\text{pH}+E^{\ominus}_{\text{Ag/AgCl}}$$

where,  $E_{\text{Ag/AgCl}}$  is the applied potential versus Ag/AgCl electrode,  $E^{\ominus}_{\text{Ag/AgCl}}$  is the standard potential of Ag/AgCl electrode (0.199 V), and  $E_{\text{RHE}}$  is the converted potential versus RHE.

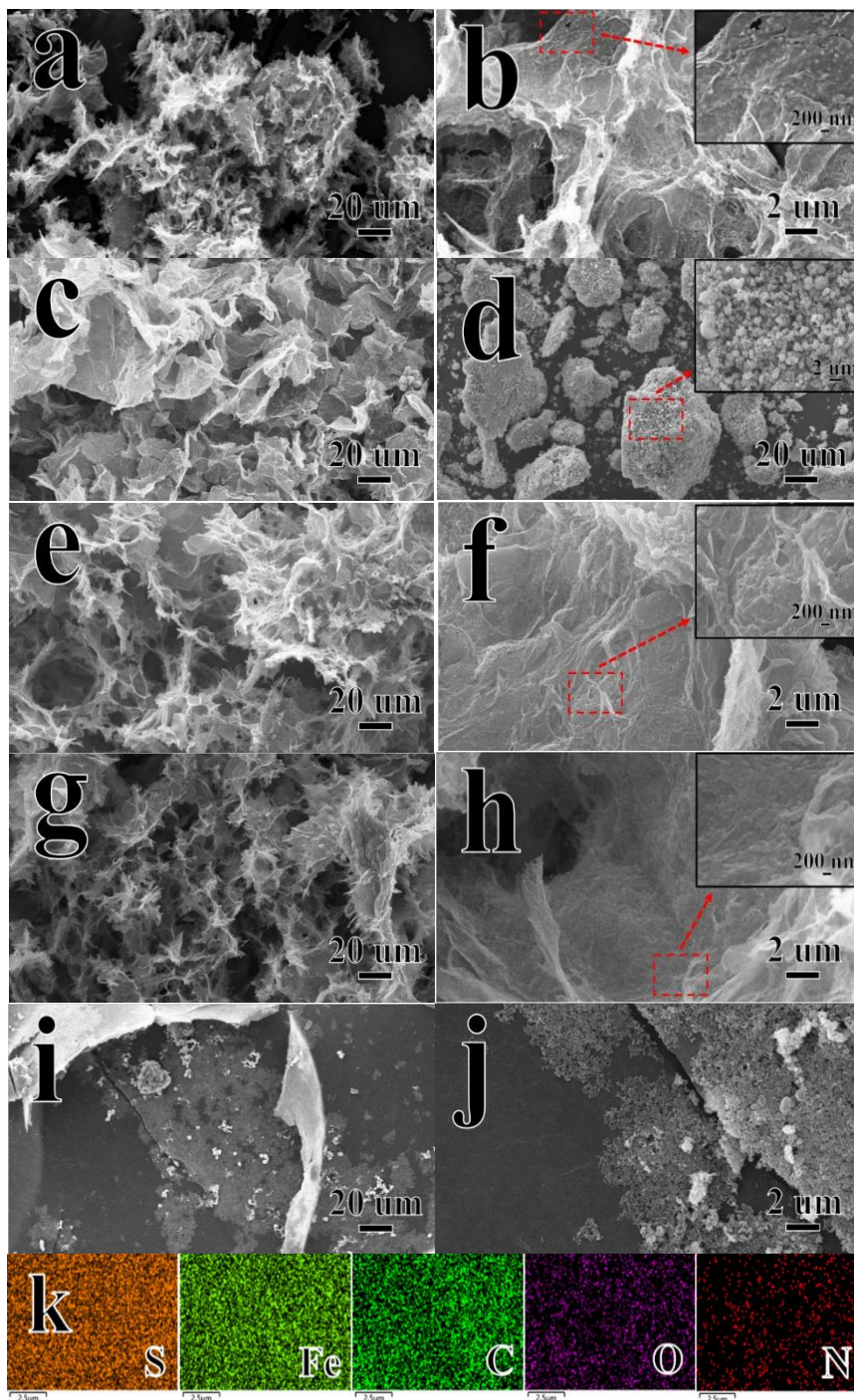
LSV test was performed at a scan rate of 5 mV $\cdot$ s $^{-1}$  in 1.0 M KOH electrolyte (pH 14). Electric impedance spectroscopy (EIS) analysis was carried out at the overpotential of 300 mV in 1.0 M KOH with the frequency range of 100 kHz to 0.1 Hz and 5 mV amplitude sinusoidal voltage as disturbance signal. Cyclic voltammetry (CV) test was adopted to calculate dynamic parameter  $C_{dl}$  (double-layer capacitance) within the scan range of 0.1–0.2 V (vs. Ag/AgCl) with different scanning rates (20, 40, 60, 80, 100, and 120 mV $\cdot$ s $^{-1}$ ). Chronopotentiometry analysis was performed at a constant current density of 100 mA $\cdot$ cm $^{-2}$  for 43200 s to characterize the stability of the electrodes.

## 3. RESULTS AND DISCUSSION

### 3.1 Morphology and composition analyses

The SEM images of Fe-S/NGF-600, bare NGF, bare Fe-S, Fe-S/NGF-400, Fe-S/NGF-800, and Fe-S/NGF are shown in Figure 2. Based on Figure 2(a), the Fe-S/NGF-600 sample has a three-dimensional porous structure with uniform pore size (about 7  $\mu$ m). Zhou et al.[27] stated that porous graphene materials have large specific surface area and high porosity, which are of great significance for enhancing electrolyte–electrode interaction and electrolyte reactant diffusion. Figure 2(b) presents the SEM image of Fe-S/NGF-600 with higher magnification. A large number of nanoparticles are

uniformly distributed on the surface of NGF. Figure 2(b) demonstrates a partially enlarged view to better observe the morphology of nanoparticles. The size of nanoparticles is uniform and about 90 nm. Yang et al.[28] reported that nanostructures can increase the specific surface area, adjust the electronic structure and hybridization to accelerate charge transfer, and optimize the binding energy between the catalyst and reaction intermediates.



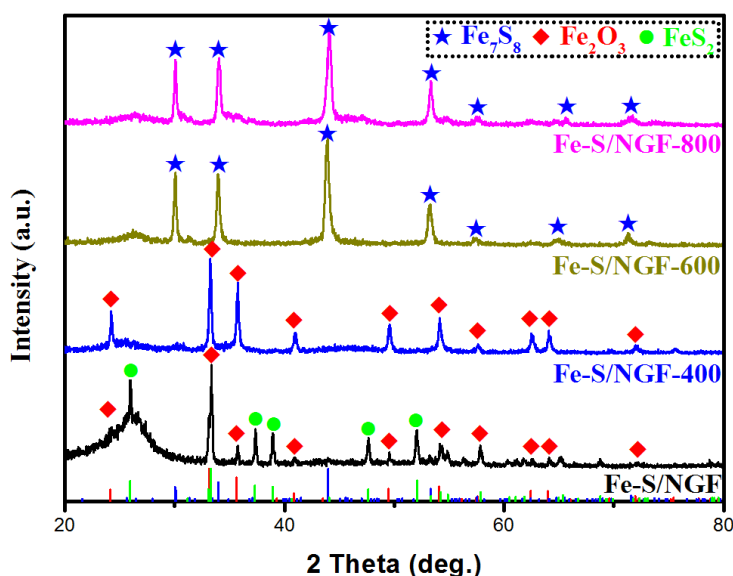
**Figure 2.** SEM images of the samples: a-b) Fe-S/NGF-600, c) bare NGF, d), bare Fe-S, (e-f) Fe-S/NGF-400, (g-h) Fe-S/NGF-800, and (i-j) Fe-S/NGF. Illustrations in all SEM images are partially enlarged. Image k is the representative EDS mapping of the sample Fe-S/NGF-600.

Figure 2(c) shows the bare NGF, which presents a porous three-dimensional structure and micro morphology comprising interlaced sheets. In the absence of the NGF substrate, Fe-S particles aggregate seriously and their size is uneven [Figure 2(d)]. The size of iron sulfide nanoparticles is about 1  $\mu\text{m}$ , which is larger than that of Fe-S/NGF-600 [Figure 2(d)]. This morphology greatly reduces the contact area between the electrolyte and electrode, thereby affecting its catalytic performance. Figures 2(e-f) and 2(g-h) show the micro morphologies of Fe-S/NGF-400 and Fe-S/NGF-800, respectively, which are similar to that of Fe-S/NGF-600. This finding is because the three groups of samples were prepared under the same hydrothermal conditions. The carbon substrate of Fe-S/NGF is flaky, and its three-dimensional structure is not obvious [Figure 2(i-j)]. The distribution of iron sulfide particles on the surface of Fe-S/NGF is uneven, and the size of particles varies greatly. Figure 2(k) displays the EDS mapping images of Fe-S/NGF-600. Fe, S, C, N, and O are uniformly distributed in the sample, indicating that Fe-S nanoparticles are uniformly covered on the surface, and N atoms are also doped into the sample.

The atomic percentages of different elements were obtained by EDS (Table 1). The content of N atom in Fe-S/NGF-600 is the highest, which indicates that more N atoms are doped in this sample. The content of S atom in Fe-S/NGF-400 is lower than that of Fe atom, while the atomic ratio of S to Fe in Fe-S/NGF-600 and Fe-S/NGF-800 is close to 1:1. This finding indicates that 600  $^{\circ}\text{C}$  is the best temperature to introduce S and N. Liu et al.[26] hypothesized that temperature may affect the doping of N atoms.

**Table 1.** Atomic percentages of different elements

	N (%)	S (%)	Fe (%)
Fe-S/NGF-400	0.97	3.05	11.38
Fe-S/NGF-600	4.37	6.61	7.35
Fe-S/NGF-800	1.02	11.78	12.19



**Figure 3.** XRD patterns of Fe-S/NGF, Fe-S/NGF-400, Fe-S/NGF-600, and Fe-S/NGF-800

Figure 3 shows the X-ray diffraction (XRD) patterns of the samples. Carbon peaks and iron compounds are present in the four groups of samples, indicating the successful preparation of composite products of iron compounds and carbon substrate. The intensity of the carbon peak ( $2\theta = 26.6^\circ$ ) of Fe-S/NGF (Figure 3) is significantly higher than that of samples prepared by CVD vulcanization. This finding indicates the uneven coverage of iron sulfide nanoparticles on the surface of the carbon substrate in Fe-S/NGF. Meanwhile, in the three other groups of samples prepared by CVD vulcanization, the coverage of iron sulfide nanoparticles on the surface of the carbon substrate is uniform, so the intensity of the carbon peak is lower. This result is consistent with the SEM analysis.  $\text{Fe}_2\text{O}_3$  and  $\text{FeS}_2$  appear simultaneously in Fe-S/NGF samples because only part of iron is sulfurized by hydrothermal vulcanization, leading to the poor catalytic performance of Fe-S/NGF. The XRD spectrum of Fe-S/NGF-400 has no iron sulfide but only  $\text{Fe}_2\text{O}_3$  because the temperature is too low and the precursor is not successfully vulcanized by CVD. Nevertheless, the XRD results indicate the successful preparation of  $\text{Fe}_7\text{S}_8$  and graphene foam composites in Fe-S/NGF-600 and Fe-S/NGF-800 samples. The diffraction peaks at  $30.03^\circ$ ,  $33.99^\circ$ ,  $43.99^\circ$ , and  $53.33^\circ$  could be indexed to the (200), (203), (206), and (220) planes of  $\text{Fe}_7\text{S}_8$  (PDF# 76-2308) with a hexagonal crystal structure. Chen et al.[18] reported that  $\text{Fe}_7\text{S}_8$  has excellent electrocatalytic properties.

XPS analysis was carried out to further investigate the composition and chemical bonding states of the samples. Figure 4 shows the XPS spectra of Fe-S/NGF-600. The XPS spectrum demonstrates the presence of S, C, O, Fe, and N in Fe-S/NGF-600 [Figure 4(e)]. Figure 4(a) shows the high-resolution XPS spectrum of Fe 2p and presents the diffraction peaks of Fe  $2p_{3/2}$  and Fe  $2p_{1/2}$ . The peaks at binding energy levels of 721.4, 712.3, and 707.9 eV correspond to  $\text{Fe}^{2+}$ , and those at 725.0 and 710.7 eV are assigned to  $\text{Fe}^{3+}$ [29]. In the high-resolution XPS spectrum of S 2p [Figure 4(b)], the peaks with binding energy levels of 164.2, 162.6, and 161.5 eV correspond to  $\text{S}^{2-}$ , while the peak at 167.8 eV may be due to the formation of  $\text{SO}_3^{2-}$  on the surface of  $\text{Fe}_7\text{S}_8$  nanoparticles by oxidation in air[29]. Figure 4(c) presents the high-resolution XPS spectrum of C 1s, which contains four peaks at 284.3, 285.0, 286.1, and 288.4 eV, corresponding to C-C/C=C bond, C-N bond, C-O bond, and C=O bond, respectively[5]. The strength of C-O bond and C=O bond is very weak. The majority of oxygen functional groups are eliminated when vulcanization is carried out at  $600^\circ\text{C}$ , which is more conducive to the incorporation of N atoms in the three-dimensional graphene foam[30].

According to the high-resolution XPS spectrum of N 1s [Figure 4(d)], the doping forms of N are pyrrolic N (399.4 eV), graphitic N (401.6 eV), and pyridinic N (398.2 eV). Nitrogen doping cannot only provide more active centers for graphene but also enhance the interaction between the carbon matrix and catalytic materials[31, 32], thereby optimizing the electron transfer kinetics in the samples. Pyridinic N can increase the number of electrocatalytic active sites in graphene, and graphite N can improve the conductivity of graphene[30, 33]. The XPS analysis results indicate the existence of  $\text{Fe}^{2+}$ ,  $\text{Fe}^{3+}$ , and  $\text{S}^{2-}$  bonds, confirming the formation of metal sulfides in the sample. The results are consistent with the XRD data.

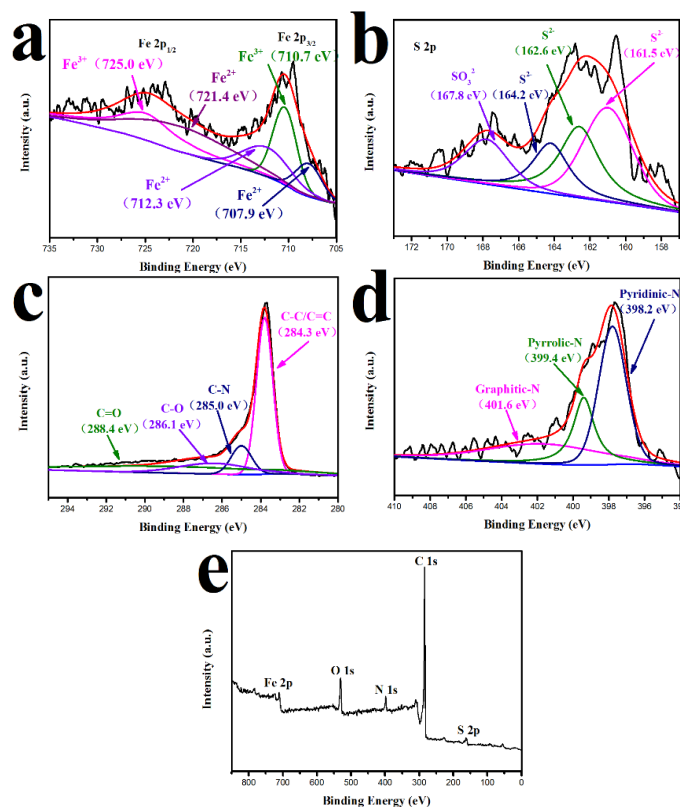


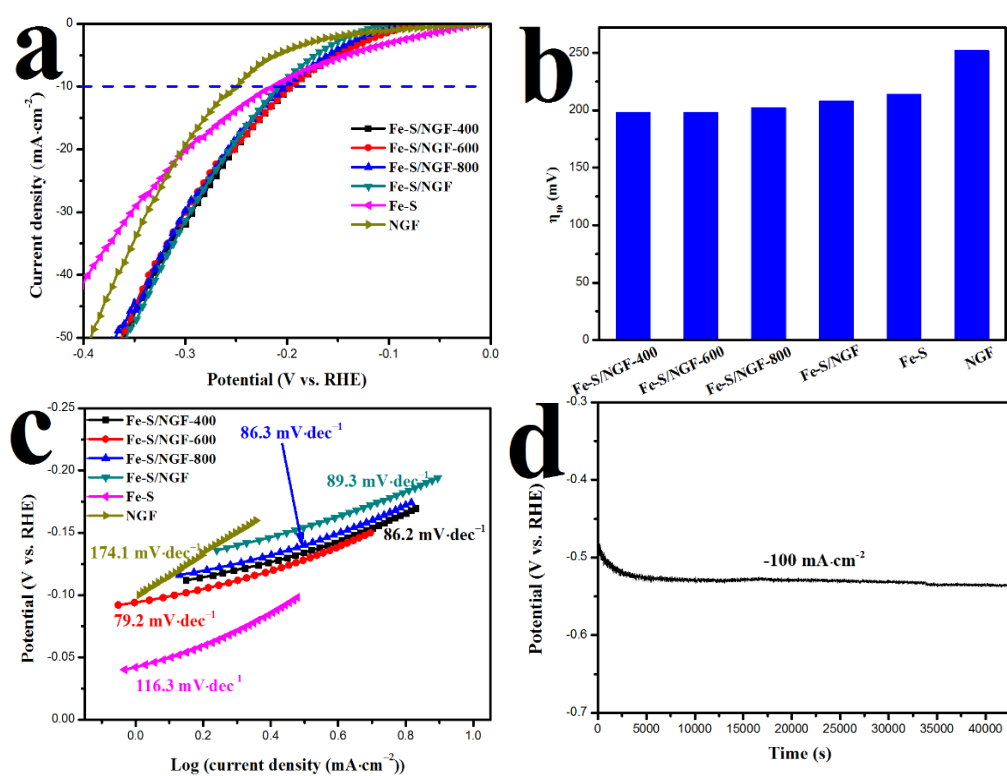
**Figure 4.** XPS spectra of Fe-S/NGF-600: a–d) high-resolution XPS spectra of a) Fe 2p, b) S 2p, c) C 1s, and d) N1s; and e) full-scan spectra

### 3.2 Electrocatalytic performance

Figures 5(a-b) show the LSV test results of the samples. The overpotential of Fe-S/NGF-600 and Fe-S/NGF-400 to reach the current density of  $10 \text{ mA}\cdot\text{cm}^{-2}$  is 197.8 mV, which is lower than those of Fe-S/NGF-800 (202.11 mV,  $10 \text{ mA}\cdot\text{cm}^{-2}$ ), Fe-S/NGF (207.92 mV,  $10 \text{ mA}\cdot\text{cm}^{-2}$ ), Fe-S (213.86 mV,  $10 \text{ mA}\cdot\text{cm}^{-2}$ ), and NGF (251.99 mV,  $10 \text{ mA}\cdot\text{cm}^{-2}$ ). This finding may be due to the high vulcanization temperature, which is not conducive to the doping of nitrogen atoms, resulting in slightly higher HER overpotential of Fe-S/NGF-800 than that of Fe-S/NGF-600. The result is consistent with the EDS data. According to the results of XRD, the overpotential of Fe-S/NGF is higher than that of Fe-S/NGF-600. The synthesis of Fe-S/NGF leads to the fact that iron sulfide is partially formed and the rest is iron oxide. The SEM results show that the three-dimensional structure of the carbon substrate is not obvious, and the distribution of nanoparticles on the surface is less and extremely uneven, leading to poor performance. The catalytic activity of Fe-S/NGF-600 for HER is higher than that of bare Fe-S and bare NGF, indicating that the composite of iron sulfide nanoparticles and the conductive matrix can effectively improve the catalytic performance.

The kinetics of HER was also studied using Tafel slope [Figures 5(c)]. The Tafel slope of Fe-S/NGF-600 is  $79.2 \text{ mV}\cdot\text{dec}^{-1}$ , which is lower than those of Fe-S/NGF-400 ( $86.2 \text{ mV}\cdot\text{dec}^{-1}$ ), Fe-S/NGF-800 ( $86.3 \text{ mV}\cdot\text{dec}^{-1}$ ), Fe-S/NGF ( $89.3 \text{ mV}\cdot\text{dec}^{-1}$ ), Fe-S ( $116.3 \text{ mV}\cdot\text{dec}^{-1}$ ), and NGF ( $174.1 \text{ mV}\cdot\text{dec}^{-1}$ ). Hence, Fe-S/NGF-600 has the fastest kinetics of hydrogen generation. The three main pathways of HER

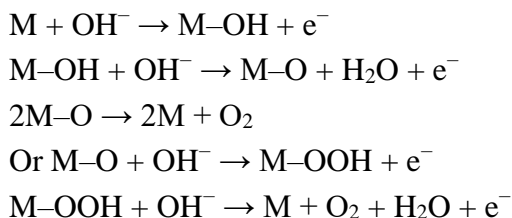
in alkaline environment are as follows[34, 35]. First, the H atom is adsorbed on the active site of the catalyst to form an adsorption intermediate [Volmer reaction with a Tafel slope of  $120 \text{ mV}\cdot\text{dec}^{-1}$  ( $\text{H}_2\text{O} + \text{M} + \text{e}^- = \text{M}-\text{H}_{\text{ads}} + \text{OH}^-$ , water discharge step)]. Subsequently,  $\text{H}_2$  is produced by Heyrovsky reaction with a Tafel slope of  $40 \text{ mV}\cdot\text{dec}^{-1}$  ( $\text{M}-\text{H}_{\text{ads}} + \text{H}_2\text{O} + \text{e}^- = \text{M} + \text{H}_2 + \text{OH}^-$ , electrochemical desorption step) or Tafel reaction with a Tafel slope of  $30 \text{ mV}\cdot\text{dec}^{-1}$  ( $2\text{M}-\text{H}_{\text{ads}} = 2\text{M} + \text{H}_2$ , chemical recombination step). In the above equations, M and  $\text{H}_{\text{ads}}$  represent the active center of the catalyst and the hydrogen atom adsorbed on the active center, respectively. The Tafel slope of Fe-S/NGF-600 is  $79.2 \text{ mV}\cdot\text{dec}^{-1}$ , indicating that the reaction pathway of HER is Volmer–Heyrovsky, and the rate control step is water discharge. Figure 5(d) shows the stability test results of Fe-S/NGF-600 under the condition of current density of  $100 \text{ mA}\cdot\text{cm}^{-2}$  for 12 h. The finding shows the excellent stability of the sample.



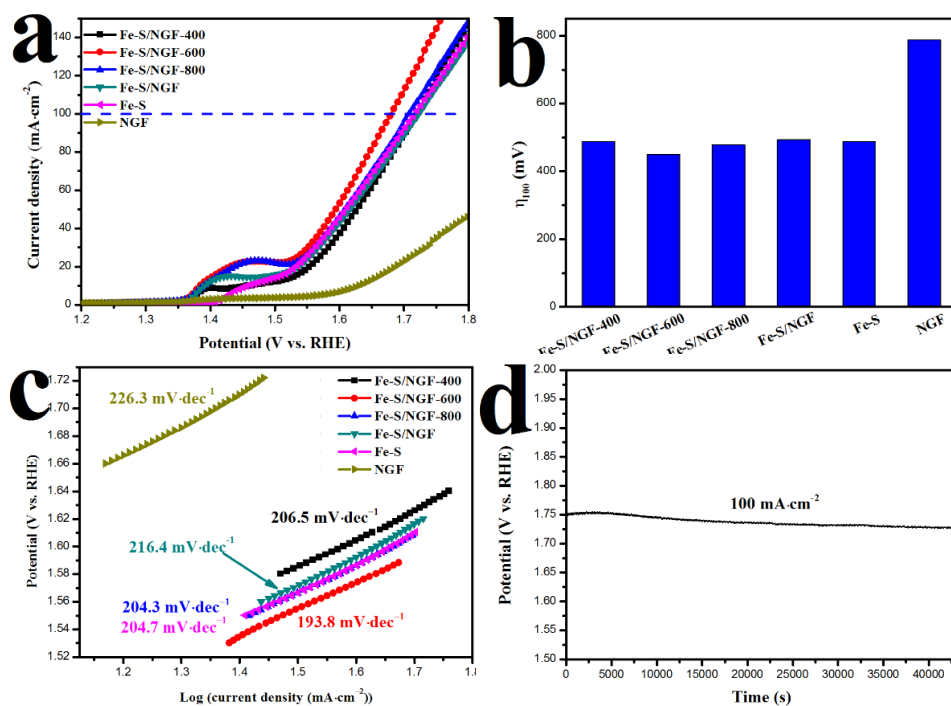
**Figure 5.** a) Polarization curves of the samples for HER at a scan rate of  $5 \text{ mV}\cdot\text{s}^{-1}$  in 1 M KOH. b) Corresponding overpotentials ( $10 \text{ mA}\cdot\text{cm}^{-2}$ ). c) Corresponding Tafel slopes. (d) Chronopotentiometry curves of the Fe-S/NGF-600 for HER under a constant current density of  $100 \text{ mA}\cdot\text{cm}^{-2}$ .

Figure 6 shows the results of the OER measurements. The current density of Fe-S/NGF-600 is higher than those of the other catalysts at a given potential. Fe-S/NGF-600 only requires an overpotential ( $\eta_{100}$ ) of 450 mV, which is remarkably lower than those of Fe-S/NGF-400 (488 mV), Fe-S/NGF-800 (478 mV), Fe-S/NGF (494 mV), Fe-S (488 mV), and NGF (478 mV) to deliver a current density of  $100 \text{ mA}\cdot\text{cm}^{-2}$  [Figures 6(a-b)]. Fe-S/NGF-600 has the best catalytic performance among all CVD vulcanization samples because iron sulfide is not formed at  $400 \text{ }^\circ\text{C}$ , while N atom doping is not favorable

at 800 °C, resulting in poor catalytic performance of the two groups of OER. In addition, the performance of Fe-S/NGF-600 is better than that of the bare Fe-S and the bare NGF, indicating that the combination of iron sulfide nanoparticles and the conductive matrix can greatly improve the catalytic performance for OER. The catalytic performance of Fe-S/NGF-600 is better than that of Fe-S/NGF. The unique three-dimensional porous structure and the uniformly distributed transition metal nanoparticles on the surface can increase the surface area in contact with the electrolyte and the number of active sites, thereby improving its catalytic performance. The pathway of OER in alkaline environment is as follows[27]:



First,  $OH^-$  is adsorbed on the surface of the catalyst (M) to form adsorption intermediate M-OH, and an electron is transferred to the electrode surface at the same time. Then, M-OH combines with another  $OH^-$  to transform into adsorption intermediate M-O and transfers an electron to the electrode surface. The conversion of M-O to oxygen follows two possible pathways. The first pathway is two M-O molecules adsorbed on the electrode directly combined to form oxygen molecules. The second one is the reaction of M-O with  $OH^-$  to form a new adsorption intermediate M-OOH, which then reacts with  $OH^-$  to produce oxygen molecules. In general, the thermodynamic barrier of the second pathway is always smaller than the first pathway[1, 27].



**Figure 6.** a) Polarization curves of the samples for OER at a scan rate of  $5 \text{ mV}\cdot\text{s}^{-1}$  in 1 M KOH. b) Corresponding overpotentials ( $100 \text{ mA}\cdot\text{cm}^{-2}$ ). c) Corresponding Tafel slopes. (d) Chronopotentiometry curves of the Fe-S/NGF-600 for OER under a constant current density of  $100 \text{ mA}\cdot\text{cm}^{-2}$ .

Figure 6(c) compares the Tafel slopes of the samples to further analyze the mechanism. The Tafel slope of Fe-S/NGF-600 is  $193.8 \text{ mV}\cdot\text{dec}^{-1}$ , which is smaller than those of Fe-S/NGF-400, Fe-S/NGF-800, Fe-S/NGF, Fe-S, and NGF. Hence, Fe-S/NGF-600 has better electrocatalytic kinetics. Figure 6(d) shows the chronopotentiometry curve of Fe-S/NGF-600 measured under a constant current density of  $100 \text{ mA}\cdot\text{cm}^{-2}$ . The potential of Fe-S/NGF-600 only changes slightly after 12 h, indicating that it has excellent stability.

The CV curves of Fe-S/NGF-600, Fe-S, and NGF at different scanning rates are shown in Figure 7(a-c). Figure 7(d) shows the linear relationship diagram of current  $\Delta j$  at different scanning rates (20, 40, 60, 80, 100, and 120  $\text{mV}\cdot\text{s}^{-1}$ ) within a certain voltage range (0.1 – 0.2 V vs. Ag/AgCl), and half of the slope is the value of  $C_{dl}$ . According to the linear relationship diagram, the  $C_{dl}$  of Fe-S/NGF-600 is  $14.56 \text{ mF}\cdot\text{cm}^{-2}$ , which is higher than those of Fe-S and NGF. This result indicates that Fe-S/NGF-600 has larger electrochemical active surface area (ESCA) than the other samples. A large ESCA is a characteristic of a nano-array structure catalyst[3].

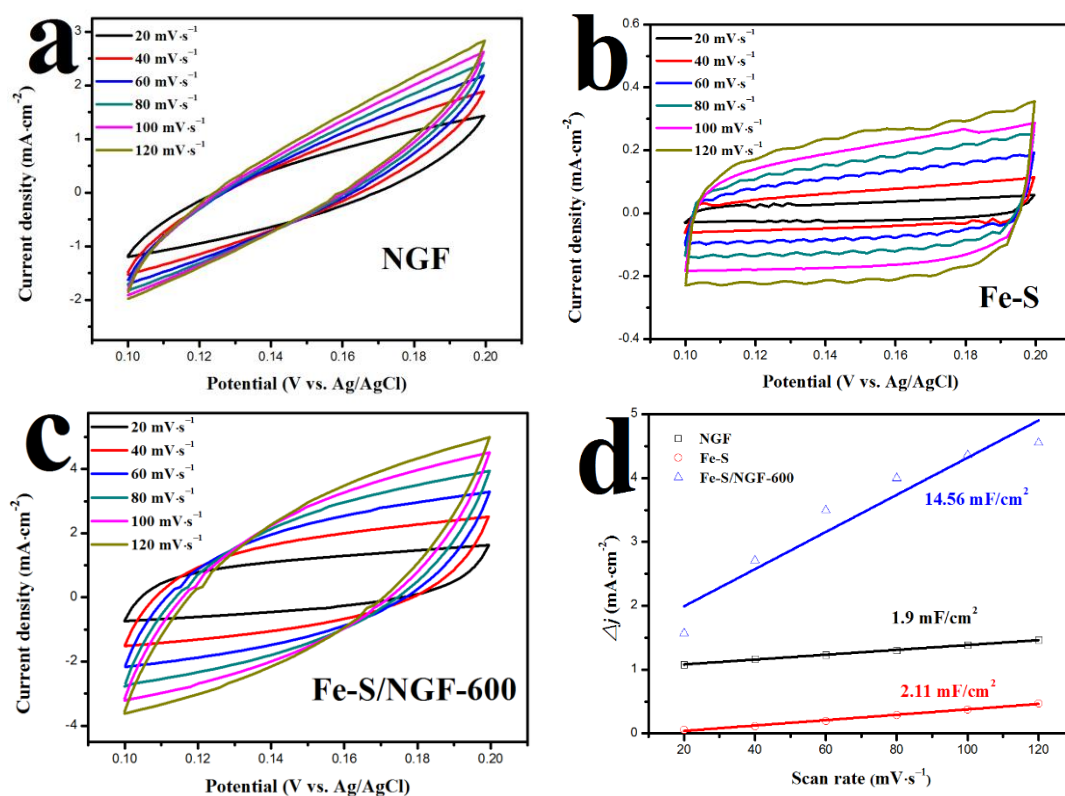


**Figure 7.** Typical cyclic voltammogram (CV) curves of a) NGF, b) Fe-S, and c) Fe-S/NGF-600 in 1 M KOH with different scan rates. d) Differences in current density of NGF, Fe-S, and Fe-S /NGF plotted against scan rates.

Figure 8 shows the Nyquist plots of the samples measured at the overpotential of 300 mV in 1.0 M KOH. The intercept between the semicircle and the real axis corresponds to solution resistance ( $R_s$ ) in the equivalent circuit diagram because of the ionic resistance of the electrolyte. A low  $R_s$  indicates

excellent conductivity. As shown in Table 2, Fe-S/NGF-600 has the lowest electrolyte resistance; thus, the desorption and adsorption of oxygen on the Fe-S/NGF-600 surface are more likely to occur[36]. This result is consistent with the previous OER catalytic performance analysis. The diameter of the semicircle is related to the charge transfer resistance ( $R_{ct}$ ) caused by redox reaction on the electrode surface. Fe-S/NGF-600 has a small  $R_{ct}$  ( $2.56 \Omega \cdot \text{cm}^{-2}$ ), which indicates that the electrode has good conductivity in the reaction[37].

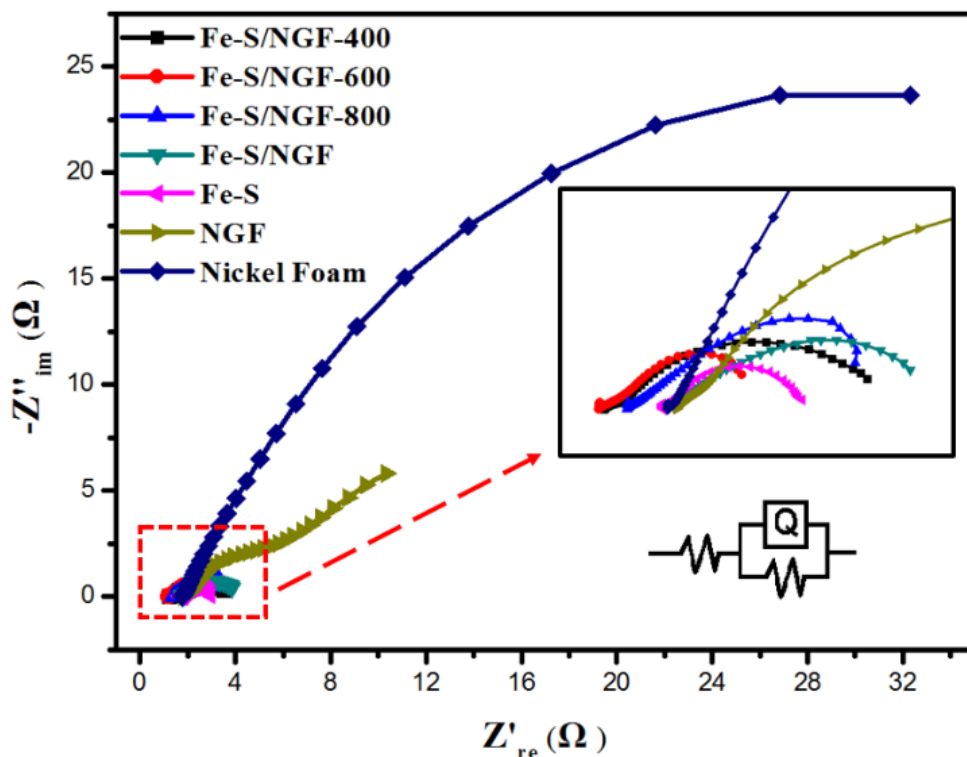


**Figure 8.** a) Nyquist plots of EIS with an overpotential of 300 mV in 1 M KOH. The insets are the equivalent model and the partial enlargement.

Electrochemical active surface area (ESCA) can be calculated from the capacitance of the double layer ( $C_{dl}$ ) by the following formula[38]:

$$C_{dl} = \left( \frac{Q}{(R_s^{-1} + R_{ct}^{-1})^{1-n}} \right)^{\frac{1}{n}}$$

ESCA can be obtained by dividing the double-layer capacitance by  $C_s$  ( $C_s$  is the specific capacitance of a flat surface of the electrode material within  $20\text{--}60 \mu\text{F} \cdot \text{cm}^{-2}$ [28]. In the present study, the test was conducted in 1 M KOH, so the  $C_s$  is equal to  $40 \mu\text{F} \cdot \text{cm}^{-2}$ [22]). In Table 2, Fe-S/NGF-600 has the largest surface active area, which is consistent with the previous CV test results.

**Table 2.** Element equivalent circuit parameters

Samples	$R_s$ ( $\Omega \cdot \text{cm}^{-2}$ )	$Q$ ( $\Omega^{-1} \cdot \text{cm}^{-2} \cdot \text{s}^{-1}$ )	$n$	$R_{ct}$ ( $\Omega \cdot \text{cm}^{-2}$ )	$C_{dl}$ ( $\mu\text{F} \cdot \text{cm}^{-2}$ )	ECSA ( $\text{cm}^2$ )
Fe-S/NGF-400	1.252	0.1459	0.5917	2.73	36053.1	901.33
Fe-S/NGF-600	1.189	0.49	0.5143	2.56	202095.3	5052.38
Fe-S/NGF-800	1.431	0.234	0.5624	3.45	73124.8	1828.12
Fe-S/NGF	1.767	0.205	0.5583	2.89	66323.3	1658.08
Fe-S	1.743	0.1582	0.7639	1.26	81182.4	2029.56
NGF	1.812	0.07828	0.5115	21.86	11234.9	280.87

The performance of Fe-S/NGF-600 as electrocatalyst for overall water splitting was studied. A two-electrode system was used, and Fe-S/NGF-600 was directly used as anode and cathode. Figure 9(a) shows the LSV test results of the sample in 1 M KOH solution with the scanning rate of  $5 \text{ mV} \cdot \text{s}^{-1}$  and the scanning range of 0.5–2.5 V.

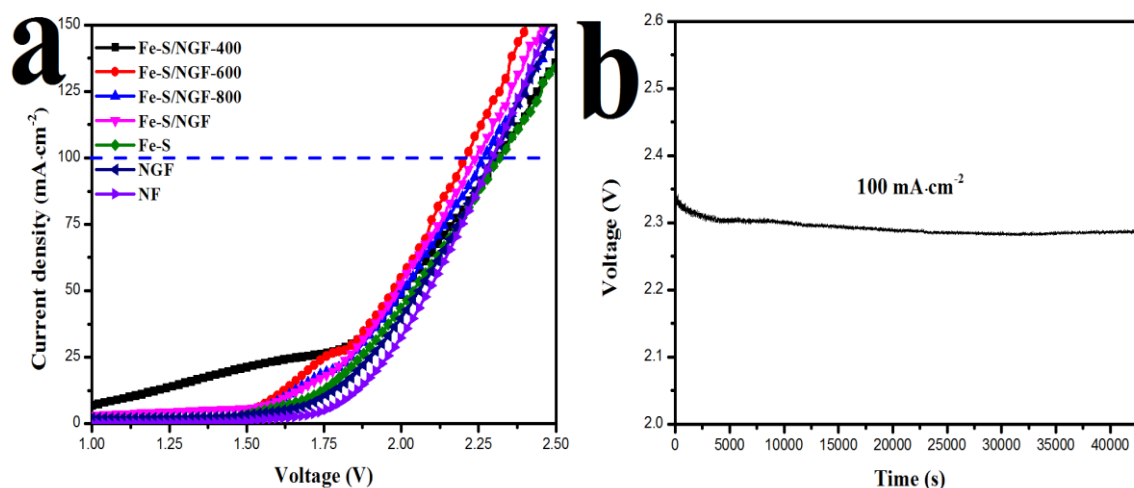


**Figure 9.** a) Polarization curves of two-electrode overall water splitting by using the prepared catalysts on nickel foam (NF) as anode and cathode at a scan rate of  $5 \text{ mV} \cdot \text{s}^{-1}$  in 1 M KOH. b) Chronopotentiometry response of Fe-S/NGF-600 carried out at  $100 \text{ mA} \cdot \text{cm}^{-2}$  current density.

As shown in Figure 9(a), Fe-S/NGF-600 has the best catalytic performance, and the current density of  $100 \text{ mA} \cdot \text{cm}^{-2}$  can be obtained by applying 2.21 V. The stability of the samples was also tested by chronopotentiometry [Figure 9(b)]. Fe-S/NGF-600 has excellent stability for long-term operation.

**Table 3.** Comparison of overpotential ( $\eta$ ) for OER and HER of transition metal-based electrocatalysts, namely, Pt/C and RuO<sub>2</sub>, in 1 M KOH alkaline electrolyte.

Electrocatalyst	HER (mV)	OER (mV)	Reference
<b>Fe<sub>7</sub>S<sub>8</sub>/NGF</b>	197.8 ( $\eta_{10}$ )	450 ( $\eta_{100}$ )	<b>this work</b>
<b>RuO<sub>2</sub></b>	/	340 ( $\eta_{10}$ )	[39]
<b>Pt/C</b>	56 ( $\eta_{10}$ )	/	[21]
<b>NiCo<sub>2</sub>O<sub>4</sub></b>	/	457 ( $\eta_{100}$ )	[40]
<b>CoP-N</b>	/	450 ( $\eta_{10}$ )	[8]
<b>Ni<sub>x</sub>S<sub>y</sub>/NGF</b>	193 ( $\eta_{10}$ )	311 ( $\eta_{10}$ )	[21]
<b>Co<sub>9</sub>S<sub>8</sub> HNSs</b>	267 ( $\eta_{10}$ )	342 ( $\eta_{10}$ )	[41]
<b>CoP</b>	159 ( $\eta_{10}$ )	400 ( $\eta_{10}$ )	[42]
<b>Co<sub>x</sub>Fe<sub>3-x</sub>O<sub>4</sub></b>	/	420 ( $\eta_{10}$ )	[43]
<b>3D Nickel</b>	/	496 ( $\eta_{50}$ )	[44]
<b>FeSe<sub>2</sub></b>	/	500 ( $\eta_{70}$ )	[45]

Table 3 summarizes the overpotentials of some transition metal-based electrocatalytic materials, namely, Pt/C and RuO<sub>2</sub>, reported in literature. Fe<sub>7</sub>S<sub>8</sub>/NGF is a potential candidate as an economic and efficient non-noble transition metal-based catalyst for OER in alkaline environment.

#### 4. CONCLUSIONS

Fe<sub>7</sub>S<sub>8</sub>/NGF electrocatalyst was successfully prepared by hydrothermal process and chemical vapor deposition. The unique three-dimensional porous structure combined with iron sulfide nanoparticles greatly increased the contact area between the catalyst and electrolyte and exposed more active sites. The residual functional groups of the graphene foam surface were removed by high-temperature vulcanization at 600 °C to enhance the conductivity of the electrocatalyst. In addition, N atoms were doped to increase the number of active sites and optimize the electron transfer process. These properties conferred Fe<sub>7</sub>S<sub>8</sub>/NGF bifunctional catalyst with excellent HER catalytic ability (197.8 mV, 10 mA·cm<sup>-2</sup>, 1 M KOH) and OER catalytic ability (450 mV, 100 mA·cm<sup>-2</sup>, 1 M KOH) as well as excellent stability. The catalyst also showed excellent overall water splitting ability, reached the current density of 100 mA·cm<sup>-2</sup>, required only 2.21 V additional applied voltage, and maintained good stability during 12 h of continuous operation. Hence, Fe<sub>7</sub>S<sub>8</sub>/NGF is expected to be a suitable alternative of noble metals for electrocatalysts because of its excellent performance, abundance of earth reserves of raw materials, simple and feasible preparation, and large-scale commercial electrolysis of water.

#### References

1. L.S. Peng, S.S.A. Shah, Z.D. Wei, *Chin. J. Catal.*, 39 (2018) 1575-1593.
2. M. Sarfraz, I. Shakir, *J. Storage Mater.*, 13 (2017) 103-122.
3. P. Guo, Y.X. Wu, W.M. Lau, H. Liu, L.M. Liu, *J. Alloys Compd.*, 723 (2017) 772-778.
4. J.Y. Kim, J.H. Choi, H.Y. Kim, E. Hwang, H.J. Kim, S.H. Ahn, S.K. Kim, *Appl. Surf. Sci.*, 359

- (2015) 227-235.
5. P.Y. Kuang, M. He, H.Y. Zou, J.G. Yu, K. Fan, *Appl. Catal., B*, 254 (2019) 15-25.
  6. Y.H. Deng, C. Ye, B.X. Tao, G. Chen, Q. Zhang, H.Q. Luo, N.B. Li, *J. Power Sources*, 397 (2018) 44-51.
  7. K.L. Yan, X. Shang, Z. Li, B. Dong, J.Q. Chi, Y.R. Liu, W.K. Gao, Y.M. Chai, C.G. Liu, *Int. J. Hydrogen Energy*, 42 (2017) 17129-17135.
  8. L. Chen, J.T. Ren, Y.S. Wang, W.W. Tian, L.J. Gao, Z.Y. Yuan, *ACS Sustainable Chem. Eng.*, 7 (2019) 13559-13568.
  9. M. Arivu, J. Masud, S. Umaphathi, M. Nath, *Electrochem. Commun.*, 86 (2018) 121-125.
  10. Y.H. Dou, T. Liao, Z.Q. Ma, D.L. Tian, Q.N. Liu, F. Xiao, Z.Q. Sun, J.H. Kim, S.X. Dou, *Nano Energy*, 30 (2016) 267-275.
  11. M.A. Ghanem, A.M. Al-Mayouf, P. Arunachalam, T. Abiti, *Electrochim. Acta*, 207 (2016) 177-186.
  12. V. Gupta, S. Gupta, N. Miura, *J. Power Sources*, 177 (2008) 685-689.
  13. S. Chen, J.J. Duan, M. Jaroniec, S.Z. Qiao, *Adv. Mater.*, 26 (2014) 2925-2930.
  14. X.W. Yu, M. Zhang, J. Chen, Y.R. Li, G.Q. Shi, *Adv. Energy Mater.*, 6 (2016) 1501492.
  15. S. Shit, S. Bolar, N.C. Murmu, T. Kuila, *ACS Sustainable Chem. Eng.*, 7 (2019) 18015-18026.
  16. X.X. Zou, Y.Y. Wu, Y.P. Liu, D.P. Liu, W. Li, L. Gu, H. Liu, P.W. Wang, L. Sun, Y. Zhang, *Chem*, 4 (2018) 1139-1152.
  17. Z.X. Jing, Q.Y. Zhao, D.H. Zheng, L. Sun, J.H. Geng, Q.N. Zhou, J.J. Lin, *J. Mater. Chem. A*, 8 (2020) 20323-20330.
  18. S.C. Chen, Z.X. Kang, X.D. Zhang, J.F. Xie, H. Wang, W. Shao, X.S. Zheng, W.S. Yan, B.C. Pan, Y. Xie, *ACS Cent. Sci.*, 3 (2017) 1221-1227.
  19. Y.G. Li, H.L. Wang, L.M. Xie, Y.Y. Liang, G.S. Hong, H.J. Dai, *J. Am. Chem. Soc.*, 133 (2011) 7296-7299.
  20. L. Liao, J. Zhu, X.J. Bian, L.N. Zhu, M.D. Scanlon, H.H. Girault, B.H. Liu, *Adv. Funct. Mater.*, 23 (2013) 5326-5333.
  21. H.Y. Zou, B.W. He, P.Y. Kuang, J.G. Yu, K. Fan, *Adv. Funct. Mater.*, 28 (2018).
  22. H. Liang, D.G. Jiang, S. Wei, X.Y. Cao, T. Chen, B.B. Huo, Z. Peng, C.W. Li, J.Q. Liu, *J. Mater. Chem. A*, 6 (2018) 16235-16245.
  23. Y.F. Zhao, X.Q. Xie, J.Q. Zhang, H. Liu, H.J. Ahn, K. Sun, G.X. Wang, *CHEM-EUR J*, 21 (2015) 15908-15913.
  24. H.R. Yuan, F. Yan, C.Y. Li, C.L. Zhu, X.T. Zhang, Y.J. Chen, *ACS Appl. Mater. Interfaces*, 10 (2018) 1399-1407.
  25. S. Umrao, T.K. Gupta, S. Kumar, V.K. Singh, M.K. Sultania, J.H. Jung, I.K. Oh, A. Srivastava, *ACS Appl. Mater. Interfaces*, 7 (2015) 19831-19842.
  26. P.B. Liu, Y.Q. Zhang, J. Yan, Y. Huang, L. Xia, Z.X. Guang, *Chem. Eng. J.*, 368 (2019) 285-298.
  27. X.J. Zhou, Z.Y. Bai, M.J. Wu, J.L. Qiao, Z.W. Chen, *J. Mater. Chem. A*, 3 (2015) 3343-3350.
  28. R. Yang, Y.M. Zhou, Y.Y. Xing, D. Li, D.L. Jiang, M. Chen, W.D. Shi, S.Q. Yuan, *Appl. Catal., B*, 253 (2019) 131-139.
  29. H. Zhang, Q.M. Gao, X.H. Tian, Z.Y. Li, P. Xu, H. Xiao, *Electrochim. Acta*, 319 (2019) 472-480.
  30. Z.H. Sheng, L. Shao, J.J. Chen, W.J. Bao, F.B. Wang, X.H. Xia, *ACS Nano*, 5 (2011) 4350-4358.
  31. M. Rahsepar, M.R. Nobakht, H. Kim, M. Pakshir, *Appl. Surf. Sci.*, 447 (2018) 182-190.
  32. S. Ratso, I. Kruusenberg, M. Vikkisk, U. Joost, E. Shulga, I. Kink, T. Kallio, K. Tammeveski, *Carbon*, 73 (2014) 361-370.
  33. Y. Zhao, R. Nakamura, K. Kamiya, S. Nakanishi, K. Hashimoto, *Nat. Commun.*, 4 (2013) 1-7.
  34. X.T. Yu, M.Y. Wang, Z. Wang, X.Z. Gong, Z.C. Guo, *Electrochim. Acta*, 211 (2016) 900-910.
  35. V. Vij, S. Sultan, A.M. Harzandi, A. Meena, J.N. Tiwari, W.G. Lee, T. Yoon, K.S. Kim, *ACS Catal.*, 7 (2017) 7196-7225.
  36. I. Herraiz Cardona, C. González Buch, C. Valero Vidal, E. Ortega, V. Pérez Herranz, *J. Power*

*Sources*, 240 (2013) 698-704.

37. L.X. Wang, Y. Li, X.C. Yin, Y.Z. Wang, L. Lu, A.L. Song, M.R. Xia, Z.P. Li, X.J. Qin, G.J. Shao, *Int. J. Hydrogen Energy*, 42 (2017) 22655-22662.
38. S.L. Wang, W.T. Li, H.S. Qin, L. Liu, Y.Y. Chen, D.H. Xiang, *Int. J. Electrochem. Sci.*, 14 (2019) 957-969.
39. C.T. Zhao, C. Yu, H.W. Huang, X.T. Han, Z.B. Liu, J.S. Qiu, *Energy Storage Mater*, 10 (2018) 291-296.
40. S. Tiwari, S. Samuel, R. Singh, G. Poillierat, J. Koenig, P. Chartier, *Int. J. Hydrogen Energy*, 20 (1995) 9-15.
41. X.Y. Ma, W. Zhang, Y.D. Deng, C. Zhong, W.B. Hu, X.P. Han, *Nanoscale*, 10 (2018) 4816-4824.
42. M.J. Liu, J.H. Li, *ACS Appl. Mater. Interfaces*, 8 (2016) 2158-2165.
43. S. Han, S.Q. Liu, S.J. Yin, L. Chen, Z. He, *Electrochim. Acta*, 210 (2016) 942-949.
44. K.L. Zhang, S.J. Deng, Y. Zhong, Y.D. Wang, J.B. Wu, X.L. Wang, X.H. Xia, J.P. Tu, *Chin. J. Catal*, 40 (2019) 1063-1069.
45. R. Gao, H. Zhang, D.P. Yan, *Nano Energy*, 31 (2017) 90-95.

© 2021 The Authors. Published by ESG ([www.electrochemsci.org](http://www.electrochemsci.org)). This article is an open access article distributed under the terms and conditions of the Creative Commons Attribution license (<http://creativecommons.org/licenses/by/4.0/>).